PROCEEDINGS, 50th Workshop on Geothermal Reservoir Engineering
Stanford University, Stanford, California, February 10-12, 2025
SGP-TR-229

Microseismic Source Mechanisms During a Utah FORGE Injection Stimulation

James Rutledge[1], Kristine Pankow[2], Peter Niemz[2], Ben Dyer[3] and Dimitrios Karvounis[3]

1 Santa Fe Seismic LLC, 4 Entrada Empinada, Santa Fe, New Mexico 87506, USA

jrutledge@sfseis.com

2 University of Utah, Seismograph Stations, Salt Lake City, Utah 84112, USA

3 Geo-Energie Suisse, Reitergasse 11, 8004 Zurich, Switzerland

Keywords: microseismic, source mechanisms, fractures, hydraulic stimulation

ABSTRACT

The Utah Frontier Observatory for Research in Geothermal Energy (FORGE) is an underground field laboratory for developing and testing technologies to facilitate the development of Enhanced Geothermal Systems (EGS). EGS involves hydraulic-fracture stimulation to create and enhance fracture systems. The initial hydraulic-fracture operations at Utah FORGE involved three injection stages conducted at or near the toe section of a deviated well completed in granitic rock at temperatures up to 210°C. Various seismic receiver configurations were used to monitor and map the induced microseismicity including deep borehole receiver strings deployed to detect and accurately map the low-magnitude ($M_w \leq -1.0$) microseismicity associated with fracture creation, stimulation and growth. Microseismic data for the third stage had the best downhole coverage. This included three vertical, multi-level downhole geophone strings providing a total of eighteen 3-component (3C) geophone receivers deployed within or just above the target reservoir. Using this three-well downhole array, we have conducted a preliminary study using waveforms of 30 high-quality events to evaluate the determination of their source mechanisms. For the 30 events, we obtained 18 double-couple solutions (shear displacement on a fracture plane). Most solutions are dominantly strike-slip with one nodal plane oriented subparallel to the plane outlined by the hypocenters and striking subparallel to the maximum horizontal stress direction. The remaining solutions indicate predominantly normal-fault displacements along similarly oriented fractures. The normal-fault displacement events occur deeper, near the base of the microseismic cloud.

1. INTRODUCTION

Monitoring for microseismicity induced by injection stimulation is critical in developing Enhanced Geothermal System (EGS) reservoirs. The primary information obtained are the cloud of event locations outlining the stimulated volume, thus providing guidance on drilling targets to connect to conductive fractures. Secondary to the event locations is obtaining the events' source mechanisms, which can give the fracture plane orientation and the sense of displacement generating the microseismic signal. Most of the deformation induced during hydraulic-fracture stimulation is associated with tensile fracture opening and growth (e.g., Maxwell et al., 2008). However, the tensile fracture growth is predominantly slow, stable and aseismic. The microseismic signals are predominantly shear displacements, interpreted to be associated with heterogeneities along the hydraulic fractures and/or the critical release of tectonic shear stresses on natural fractures (e.g., Staněk and Eisner, 2017; Rutledge et al., 2018). Source mechanism results can be useful in discerning how much natural fractures play a role in the stimulated rock volumes and can provide some guidance in modeling the fracture networks created and enhanced.

We have conducted a preliminary study on microseismic source mechanisms from the 2022 stimulations at the Utah Frontier Observatory for Research in Geothermal Energy (FORGE). Figure 1 shows the stage-3 source locations determined by Dyer et al. (2023a; 2023b). Stage 3 was one of three stages initially pumped along the toe section of well 16A in the Spring of 2022. Of the first three stages completed, stage 3 had the best downhole receiver coverage for monitoring the microseismicity. This included three vertical, multi-level downhole geophone strings providing a total of eighteen 3-component (3C) geophone receivers deployed within or just above the target reservoir (Figure 1). Wells 58 and 78B each had 700 ft long, 8-level, digital, 3C strings placed approximately 1500 and 2000 ft above the 16A injection depths. The depth placements of the digital string were limited by their temperature specifications. A two-level analog string was placed in well 56 with the lower geophone set at reservoir depth and the upper receiver anchored 1000 ft above (Figure 1).

2. DATA AND ANALYSIS

Figure 2 shows the stage-3 event locations in greater detail. A total fluid volume of 3016 barrels was pumped at rates up to 35 barrels/minute. The treatment included a slickwater pad followed by a low-viscosity cross-linked gel and small concentrations of micro-proppant. For this study, we chose 30 high signal-to-noise events, their source locations highlighted as the red symbols in Figure 2, to evaluate the determination of their source mechanisms.

Obtaining seismic source mechanisms essentially involves resolving the source radiation patterns. With extensive receiver configurations, this can often be done using the P-wave polarities and amplitudes alone. Sparse receiver coverage, such as provided by the Utah FORGE downhole network, requires resolving the relative radiation patterns of the P- and S-wave phase amplitudes and their

first motions (polarities). Using the program FOCMEC (Snoke, 2003), we solved for stable double-couple fault plane solutions using a combination of P-, SH-, and SV-phase first motions and the amplitude ratios of SH/P, SV/P and SH/SV obtained from the sparse array. Double-couple solutions describe shear displacement on a fracture plane, rather than more generalized moment tensor solutions that could include, for example, tensile crack opening or closing and volumetric components of deformation. Niemz et al. (2024) have conducted a preliminary moment tensor analysis of Utah FORGE microseismicity from the recent 2024 stimulations (Niemz et al., 2025) using an extensive, high-resolution surface and near-surface receiver array. They do resolve significant non-double-couple components, but still, the predominant components of displacements for their solutions are double couple (shear) mechanisms.

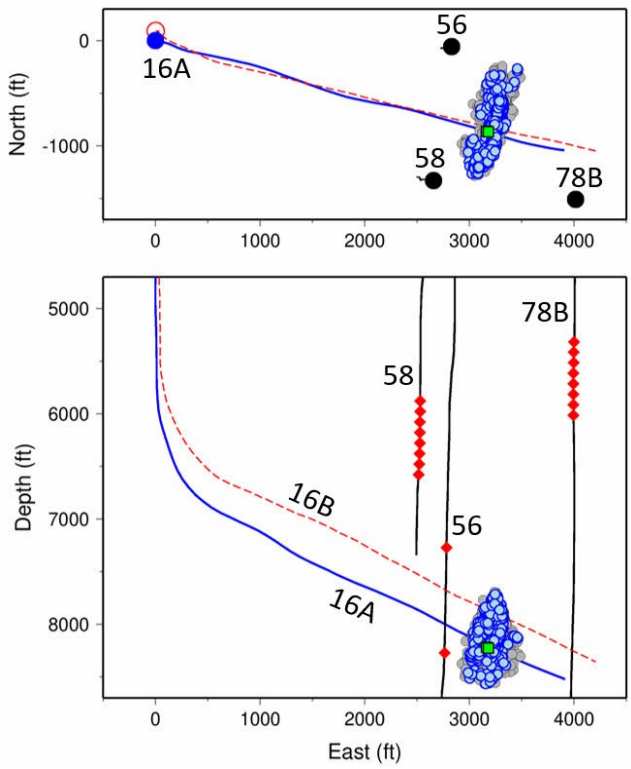

Figure 1: Microseismic event locations for stage 3 completed in well 16A (Dyer et al., 2023a; 2023b). The entire population of located events is shown in gray, consisting of 5283 events with moment magnitudes (M_w) ranging from -2.0 to 0.6. The events shown blue are a subset (1120 events) with higher magnitudes, Mw ≥ -0.85. The 3-component geophone receivers are shown as red diamonds in monitor wells 58, 78B and 56. The location of the 16A stage-3 perforation interval, which was 20 ft long, is shown with the green square. The 16B well, shown as a red dashed line, was drilled after the stage-3 stimulation.

In preparing the data, we determined the 3C geophone orientations using downhole string shots and wellbore perforation shots fired in well 16A. We also used the event source locations, which were determined using the travel times from the 3-well array (Dyer et al., 2023a), to improve the relative receiver orientations. The larger azimuthal spread of the event locations also helped to identify, and remove from consideration, poor receiver response caused by some horizontal channels being under-amplified. The receiver waveform data were rotated to P, SH, and SV phases and the three phase polarities were precisely picked. Coherency across the oriented vertical strings allowed SV and SH phases to be identified and picked consistently with confidence. The distinction and combination SH/P and SV/P amplitude ratio data are especially helpful in constraining the solutions using the sparse receiver coverage. SH/P helps constrain fault plane strike but is insensitive to fault dip. Conversely, SV/P helps constrain fault dip but is insensitive to fault strike (e.g., Figure 3).

3. RESULTS

For the 30 events examined, we obtained convergence for 18 solutions. Figure 4 describes the graphical presentation of the fault plane solutions and, for the example displayed, also shows some of the corresponding waveforms from which the input data are obtained. The waveforms show characteristics qualitatively consistent with the double-couple solution. For example, the receivers in well 78B are located near or on a P-nodal plane (Figure 4 left) and, as expected, show low-amplitude P waves (Figure 4 right). Conversely, the receivers in well 58 are located nearer to the center of the dilational quadrant (towards the P axes of Figure 4) and correspondingly show higher P-wave amplitudes relative to the S phases (Figure 4 right).

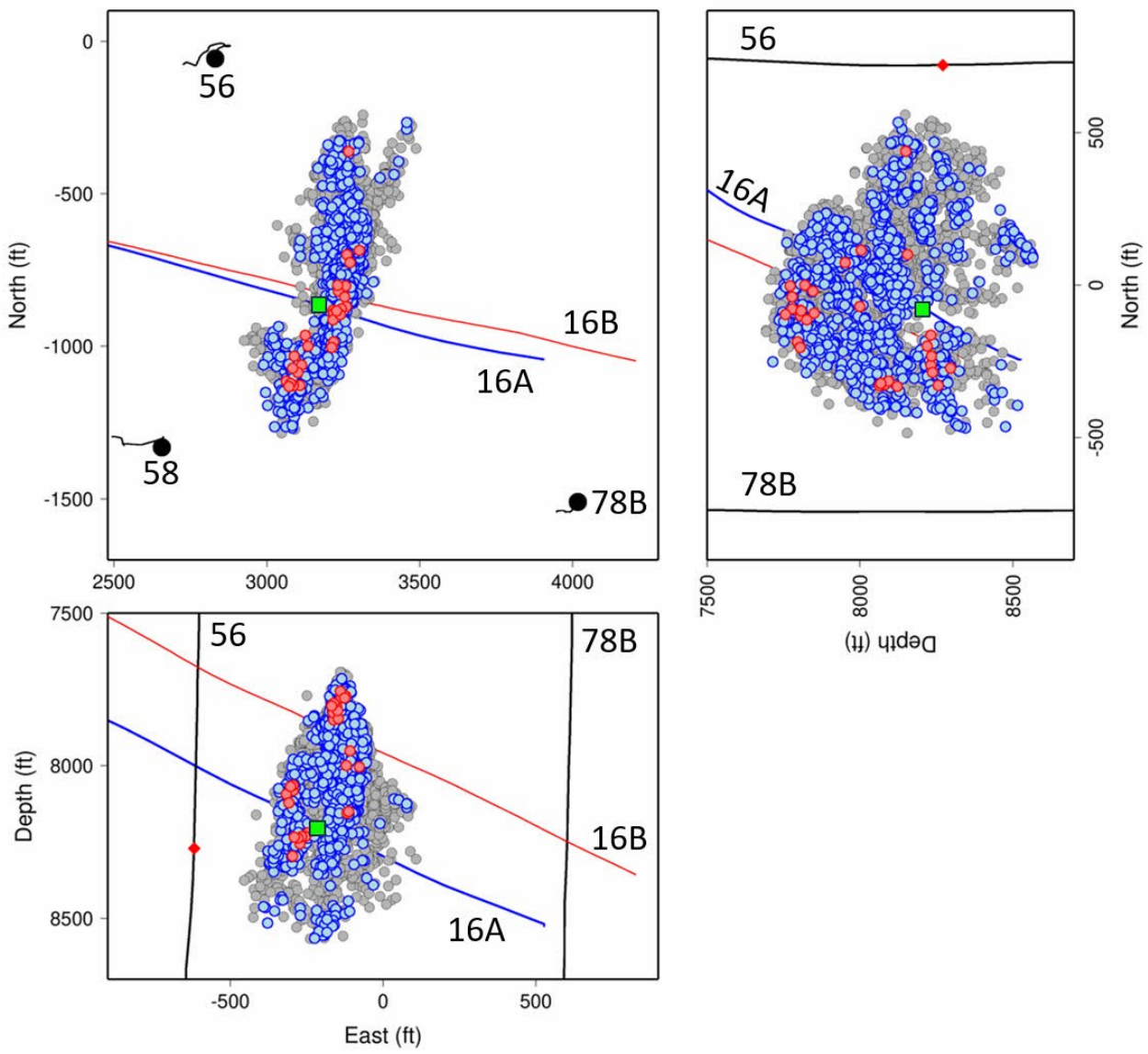

Figure 2: Details of microseismic event locations for stage 3 completed in well 16A. As in Figure 1, the entire population of located events is shown in gray, consisting of 5283 events with moment magnitudes (M_w) ranging from -2.0 to 0.6. The events shown blue are a subset (1120 events) with higher magnitudes, Mw ≥ -0.85. Thirty events with high signal-to-noise ratios were considered for source mechanism analysis in this study and are displayed red. The stage-3 perforation interval was 20 ft long, and is located at the green square. The 16B well, shown as a red trace, was drilled after the stage-3 stimulation.

Of the 18 solutions obtained, 13 show no discrepant P-wave first motions (Figures 5 and 6). Most solutions are dominantly strike-slip with one nodal plane oriented subparallel to the plane outlined by the hypocenters (Figure 5). All show right-lateral strike-slip on the planes striking close to north-south. The remaining solutions are predominantly normal-fault displacements (Figure 6). Of the 30 events examined, the set of normal-fault solutions occurs deepest, clustered near the base of the microseismic cloud (Figure 6).

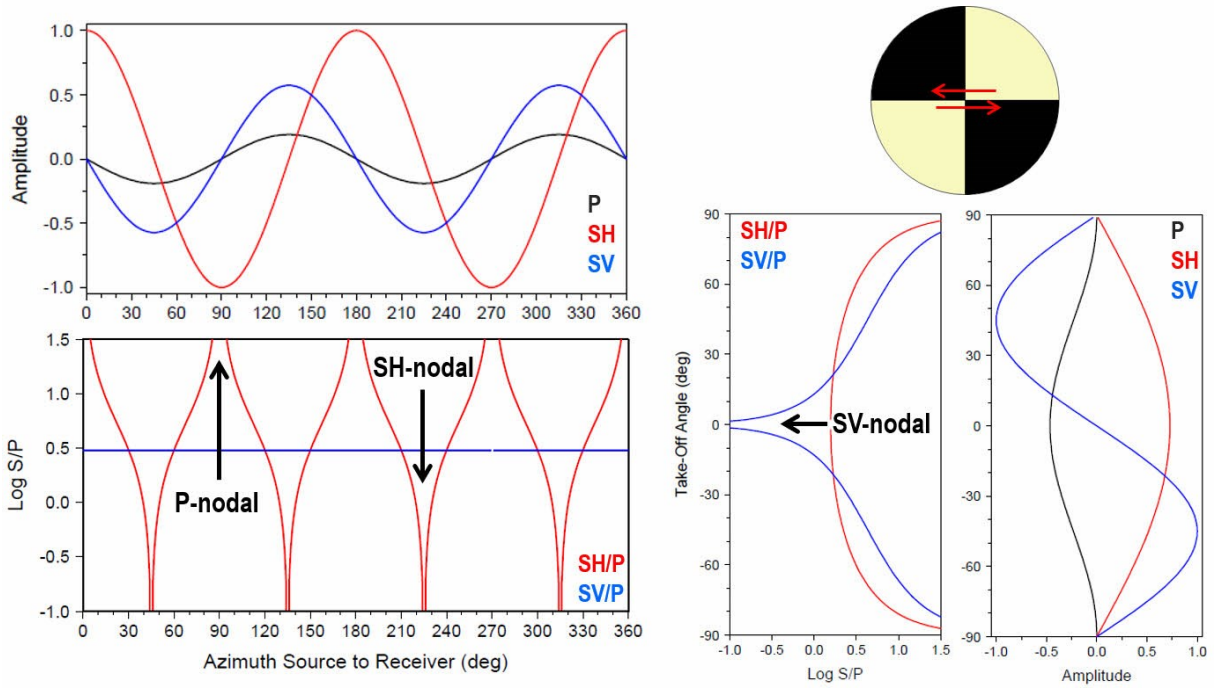

Figure 3: Theoretical relative phase amplitudes and amplitude ratios for the strike-slip mechanism shown upper right, as a function of azimuth from source to receiver (left panels) and as a function of the take-off or inclination angle from source to receiver (right panels). SH/P is sensitive to the azimuth angle or fault strike (left) but insensitive to take-off angle or fault dip (right). Conversely, SV/P is sensitive to take-off angle or fault dip (right) but insensitive to fault strike (left). Some nodal angles are labeled. For the azimuth view (left), the curves are calculated for a take-off angle 35° up from horizontal. For the take-off angle view (right), the curves are calculated at a source-to-receiver azimuth of 35°. These angles were chosen to stay away from nodal planes. For this display, the relative P- and S-amplitude scaling factor of the P- to S-velocity ratio cubed $(Vp/Vs)^3$ is set to 4.9 (Aki and Richards, 1980).

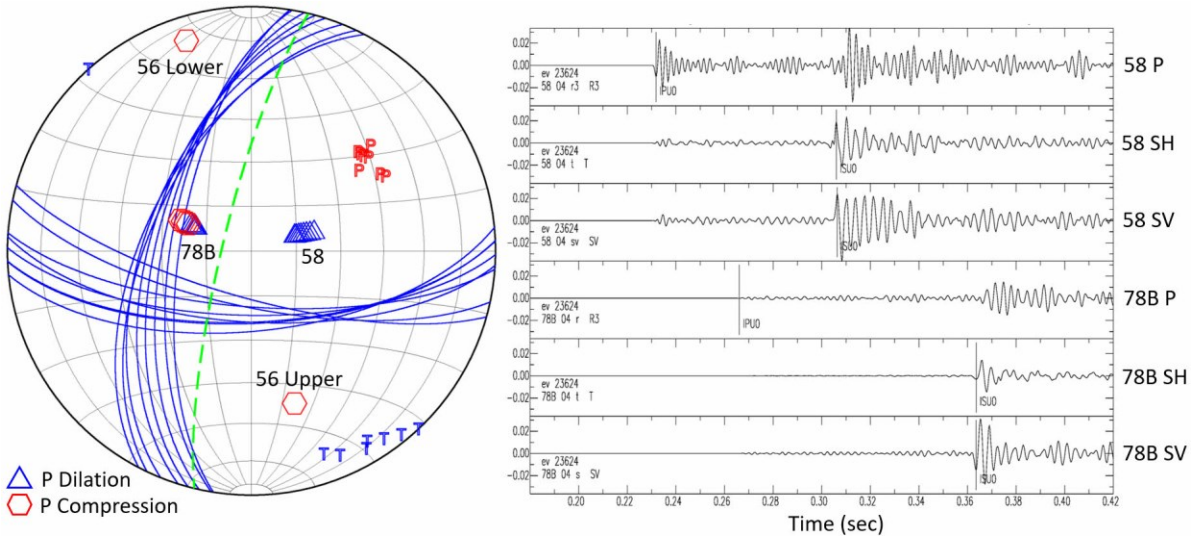

Figure 4: (Left) Example of a fault plane solution for a stage-3 event. The fault plane solution display is a lower hemisphere projection. The green dashed plane is the orientation of the event hypocenter plane, determined from principal component analysis of the event locations. The P-wave first motions are displayed for the three monitor wells. The multiple nodal planes show the range of good data fit. The corresponding P and T axes are also displayed; the P-axes are in the dilational quadrants. The strike-slip motion on the N-S nodal planes is right lateral. (Right) Waveforms for the resolved P, SH and SV components at midlevel of the vertical strings in wells 58 and 78B. Scaling is uniform across all traces to display the relative phase amplitudes.

After the completion of stimulation stages 1, 2 and 3, well 16B was drilled to target and intersect the microseismic event clouds (e.g., Figures 1 and 2). Figure 7 show the fracture orientations and their features obtained from a formation microresistivity imaging (FMI) log as well as from core recovered from the 16B interval intersecting the cloud. It is not clear if these features were created by the injection stimulation and/or if they were natural features existing before the stimulation (Jones et al., 2025). In any case, the orientations of these fractures are consistent with the orientation of the microseismically activated fractures (Figures 7 and 5). The 16A and 16B FMI logs show drilling-induced tensile fractures striking dominantly NNW-SSW, aligned with the hypocenter trend (N14°E) and the strike-slip fault plane solutions (Figures 8 and 5). The FMI continuous fractures in 16A are interpreted to be natural and are oriented dominantly near vertical and striking about N45°E (Figure 8c). Taking the prevalent drilling-induced fractures to be aligned with the maximum horizontal stress orientation (SHmax), the natural fractures identified in 16A are optimally oriented, and hence pressure sensitive for strike-slip shear failure (rotated 25° to 30° from SHmax, Figure 8). Our preliminary source mechanism work suggests an absence of microseismic shearing on the favorably-aligned natural fractures during the stage-3 stimulation. Further, this would suggest that the natural fractures are not playing a significant role in the fracture propagation and fluid pathing for the stage-3 stimulation.

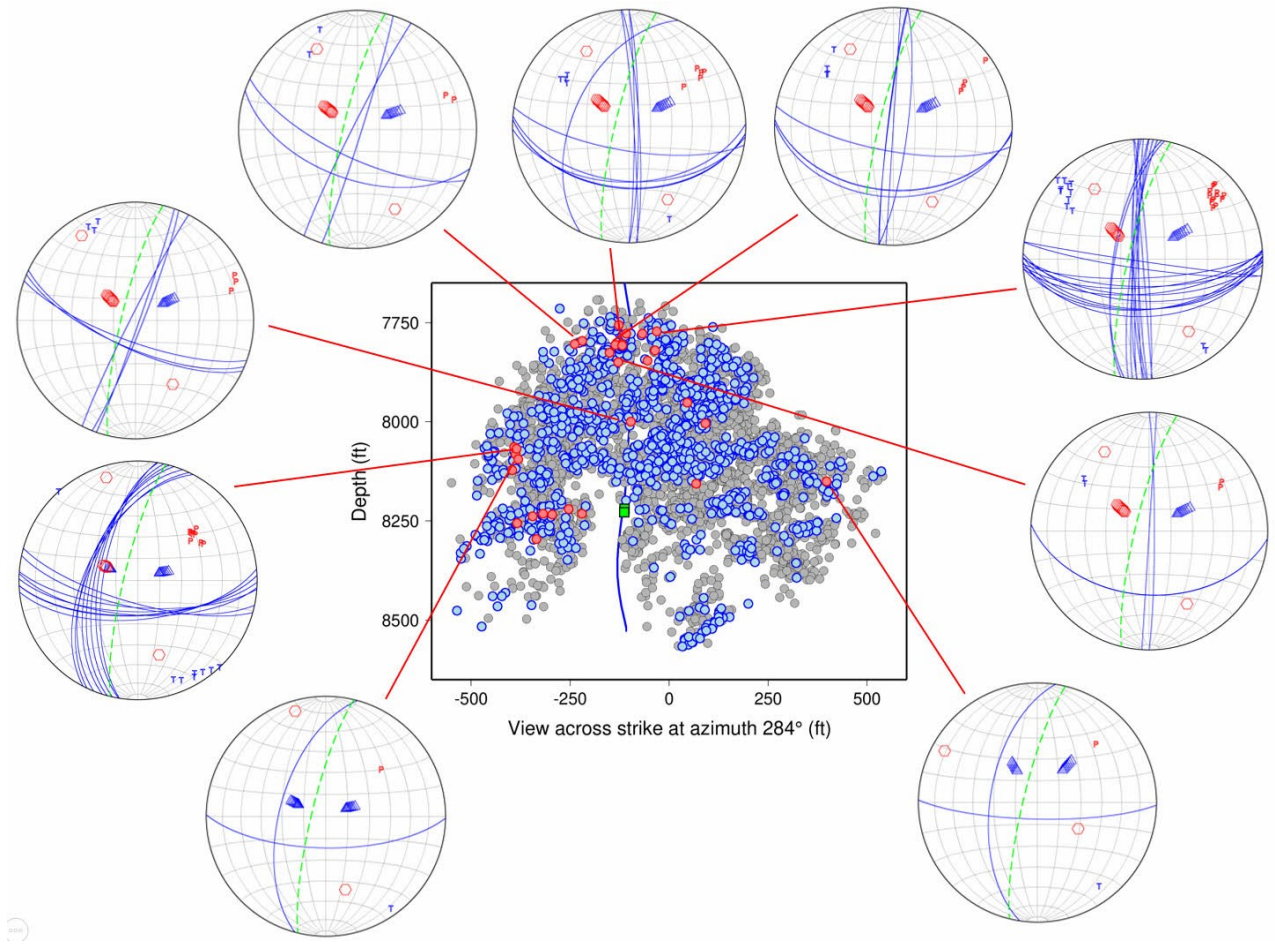

Figure 5: Strike-slip dominant events and their locations in the microseismic cloud. See Figure 4 for description of the fault plane solutions. The event location map is a depth view looking perpendicular (at azimuth 284°) to strike of the hypocenter trend (N14°E). The events shown red were selected for the source mechanism analysis. See Figure 2 for description of the event locations. Injection well 16A is the blue trace; the green square marks the perforation interval.

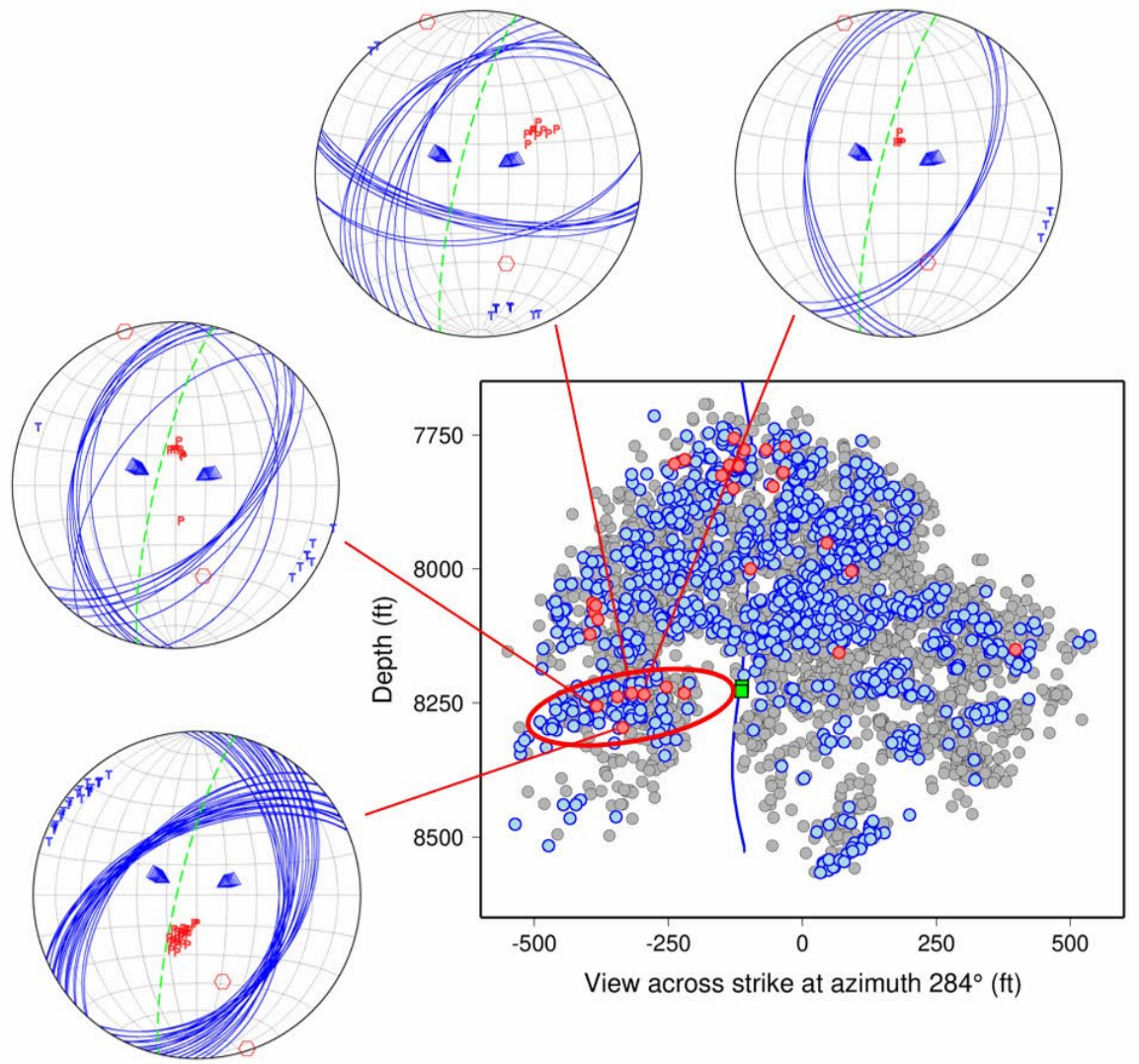

Figure 6: Normal-fault dominant events and their locations in the microseismic cloud. The event location map is a depth view looking perpendicular (at azimuth 284°) to strike of the hypocenter trend (N14°E).

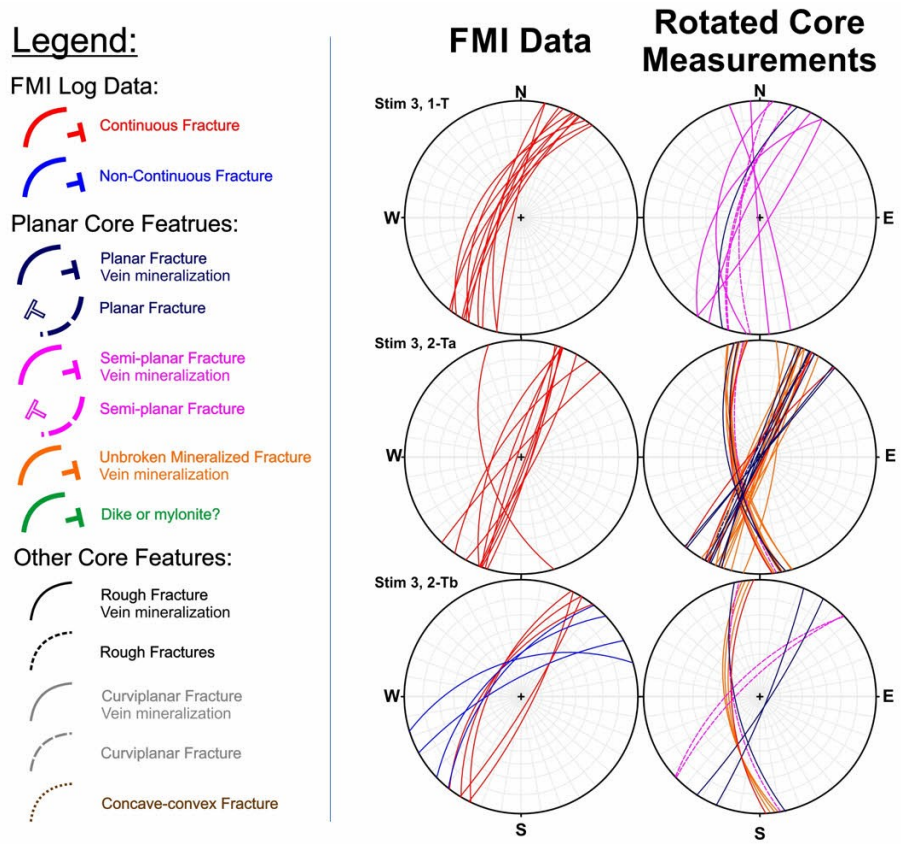

Figure 7: Fracture features identified in a formation microresistivity imaging (FMI) log and from recovered core, both obtained in well 16B over the interval where the well intersected the stage-3 microseismic cloud. The stereonets are lower hemisphere, equal angle, polar grid displays. Figure after Jones et al. (2025).

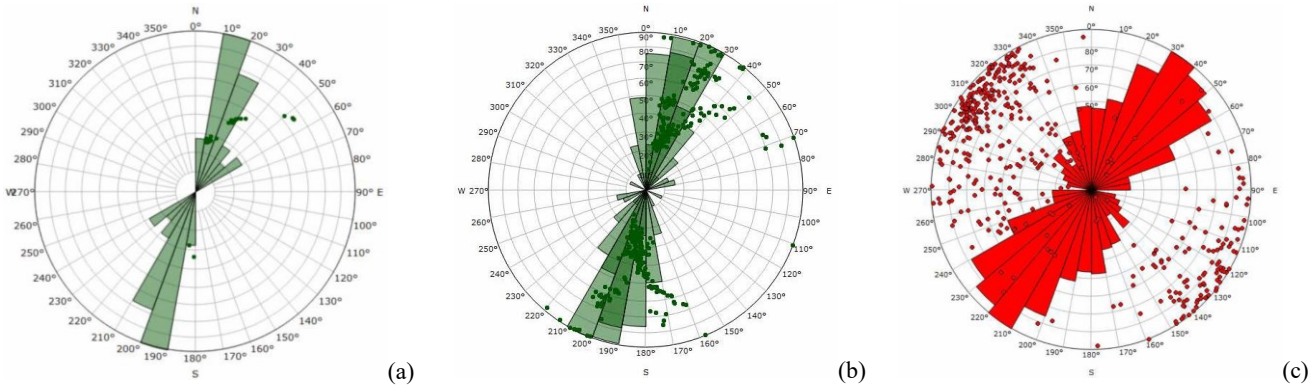

Figure 8: Fracture poles and strike distributions (a) 16B tensile drilling-induced fractures, interval 8578 to 10839 ft measured depth (MD), (b) 16A tensile drilling-induced fractures, interval 5134 to 10860 ft MD, (c) 16A conductive continuous fractures, n=431, interval 5134 to 10860 ft MD. Displays are upper hemisphere Schmidt stereonets.

4. CONCLUSIONS

We conducted a preliminary study of determining microseismic source mechanisms using a three-well array of downhole geophone strings deployed during the Utah FORGE, well 16A, stage-3 injection stimulation. Our results show predominantly strike-slip shearing along fractures subparallel to the event trend and to the strike of SHmax. For stage 3, the results suggest that the prevalent natural fracture population are not playing a significant role in the fracture propagation and fluid pathing during the injection stimulation. We are in the process of extending the analysis to a much larger subset of the microseismic events to determine if the same patterns of induced shearing persist throughout the stage-3 stimulated rock volume.

ACKNOWLEGDMENTS

We thank Aleta Finnila and Clay Jones for help with figures and guidance on the borehole fracture analysis at Utah FORGE.

REFERENCES

Aki, K., and Richards, P.G.: Quantitative seismology, theory and methods, W. H. Freeman and Company, (1980).

Dyer, B., Karvounis, D., Bethmann, F.: Microseismic event catalogues from the well 16A(78)-32 stimulation in April, 2022 in Utah FORGE., ISC Seismological Dataset Repository, https://doi.org/10.31905/52CC4QZB, (2023a).

Dyer, B.C., Bethmann, F., Karvounis, D., Meier, P., Pankow, K., Wannamaker, P., Moore, J., Rutledge, J., and Ammon, A.: Innovative microseismic monitoring tools and configurations for geothermal applications, Proceedings World Geothermal Congress, Beijing, China, (2023b).

Finnila, A., and Jones, C.: Updated reference discrete fracture network model at Utah FORGE, Proceedings, 49th Workshop on Geothermal Reservoir Engineering, Stanford University, Stanford, CA (2024).

Jones, C., Simmons, S., Moore, J.: Characterization of drill core from stimulated crystalline reservoir rock following hydraulic fracturing at the Utah FORGE Geothermal Test Site, Proceedings, 50th Workshop on Geothermal Reservoir Engineering, Stanford University, Stanford, CA (2025).

Maxwell, S. C., Shemeta, J, Campbell, E., and Quirk, D.: Microseismic deformation rate monitoring: Proceedings of the 2008 Society of Petroleum Engineers Annual Technical Conference, Paper 116596, (2008).

Niemz, P., Rutledge, J., Petersen, G., Finger, C., and Pankow, K.: DC or non-DC? Exploring uncertainties and resolution limitations for source mechanism studies at Utah FORGE, 39th General Assembly of the European Seismological Commission, Corfu, Greece, (Abstract), Sep 22-27, (2024).

Niemz, P., Pankow, K., Isken, M.P., Whidden, K., McLennan, J., Moore, J.: Mapping fracture zones with Nodal geophone patches: Insights from induced microseismicity during the 2024 stimulations at Utah FORGE, Seismological Research Letters, doi: https://doi.org/10.1785/0220240300, (2025).

Rutledge, J., Leaney, S., Best, J., Craven, M., and Swafford, L.: High-resolution microseismic source locations and moment tensor solutions from the Permian Basin, Society of Exploration Geophysicists Technical Program Expanded Abstracts, 3022-3026, doi: 10.1190/segam2018-2997290.1. (2018).

Snoke, J.A.: FOCMEC: FOCal MEChanism determinations, *in* International Handbook of Earthquake and Engineering Seismology (eds., Lee, W.H.K., Kanamori, H., Jennings, P.C., and Kisslinger, C.), Academic Press, San Diego, (2003).

Staněk, F., and Eisner, L.: Seismicity induced by hydraulic fracturing in shales: A bedding plane slip model: Journal of Geophysical Research: Solid Earth, 122, 7912–7926, https://doi.org/10.1002/2017JB014213, (2017).